

Theoretical analysis of thermal boundary conductance of MoS₂-SiO₂ and WS₂-SiO₂ interface

Zhun-Yong Ong*

*Institute of High Performance Computing, A*STAR, Singapore 138632, Singapore*

Yongqing Cai

*Joint Key Laboratory of the Ministry of Education,
Institute of Applied Physics and Materials Engineering, University of Macau, Taipa, Macau, China*

Gang Zhang

*Institute of High Performance Computing, A*STAR, Singapore 138632, Singapore*

Yong-Wei Zhang

*Institute of High Performance Computing, A*STAR, Singapore 138632, Singapore*

(Dated: October 11, 2021)

Understanding the physical processes involved in interfacial heat transfer is critical for the interpretation of thermometric measurements and the optimization of heat dissipation in nanoelectronic devices that are based on transition metal dichalcogenide (TMD) semiconductors. We model the phononic and electronic contributions to the thermal boundary conductance (TBC) variability for the MoS₂-SiO₂ and WS₂-SiO₂ interface. A phenomenological theory to model diffuse phonon transport at disordered interfaces is introduced and yields $G = 13.5$ and 12.4 MW/K/m² at 300 K for the MoS₂-SiO₂ and WS₂-SiO₂ interface, respectively. We compare its predictions to those of the coherent phonon model and find that the former fits the MoS₂-SiO₂ data from experiments and simulations significantly better. Our analysis suggests that heat dissipation at the TMD-SiO₂ interface is dominated by phonons scattered diffusely by the rough interface although the electronic TBC contribution can be significant even at low electron densities ($n \leq 10^{12}$ cm⁻²) and may explain some of the variation in the experimental TBC data from the literature. The physical insights from our study can be useful for the development of thermally aware designs in TMD-based nanoelectronics.

I. INTRODUCTION

Atomically thin two-dimensional (2D) transition metal dichalcogenide (TMD) semiconductors such as MoS₂ and WS₂ hold great potential for the development of next-generation electronic devices^{1,2}. At the nanoscale, high power densities in these devices require efficient thermal management crucial for optimal device performance, with the thermal boundary conductance (TBC) of the 2D crystal-substrate interface playing a key role in the dissipation of excess Joule heat^{3,4}. Therefore, clearer insights into the role of the different physical mechanisms underlying the TBC of the TMD-substrate interface may lead to superior thermally aware TMD-based nanoelectronic device designs.

One widely studied mechanism is the van der Waals coupling between the phonons of the 2D crystal and its substrate which is believed to be the dominant component in the overall TBC⁴. The phononic TBC (G_{ph}) has been estimated using molecular dynamics (MD) simulations^{5,6}, elasticity theory⁷⁻⁹ and density functional theory-based models¹⁰. Another mechanism of heat dissipation is through the inelastic scattering of electrons in the 2D crystal by dipoles in the dielectric substrate, a phenomenon known widely as “remote phonon (RP) scattering” or “surface optical phonon scattering”¹¹⁻¹⁴. This inelastic scattering mechanism, which plays an important role in limiting the electron mobility in TMDs^{15,16}, also underlies the electronic TBC (G_{el}) and depends strongly on the electron or hole density. Although it is predicted to be insubstantial for heat dissipation in graphene^{17,18}, the contribution from RP scattering may be significant and comparable to the phononic TBC for MoS₂ and WS₂¹⁹.

Nonetheless, even though the phononic TBC has been studied using various theoretical methods, it is useful to have a model that relates G_{ph} to the fundamental elastic properties of the 2D crystal and its substrate while accounting for quantum statistics at low temperatures. One such theory that is based on coherent flexural phonons⁷ and developed in Ref.⁸ yields relatively accurate values for the graphene-SiO₂ interface^{8,9} and also predicts a modest room-temperature phononic TBC of ~ 3.1 MW/K/m² for the MoS₂-SiO₂ interface, in good agreement with earlier published data²⁰ but considerably smaller than later more accurately measured TBC values^{21,22} in the range of 10 to 15 MW/K/m². This substantial discrepancy necessitates a relook of the heat dissipation mechanisms at the TMD-substrate interface.

In our paper, we model the relative contribution of the different physical mechanisms to the overall TBC of the MoS₂-SiO₂ and WS₂-SiO₂ interface. Our objective is to understand how these mechanisms (e.g. coherent vs. diffuse phonon transport and the electron density dependence of G_{el}) lead to the variability in their TBC. We revisit the phononic TBC problem and introduce a phenomenological *diffuse* phonon theory that is more suitable for atomically disordered interfaces and allows us to model the effect of disorder on the TBC. To understand its difference to the coherent theory, we compare the TBC predictions from the coherent and diffuse phonon models with data from experiments and MD simulations. We also compare the phononic contribution (coherent or diffuse) to the electronic contribution in the TBC. Finally, we use the combined electronic and phononic BC results ($G = G_{\text{el}} + G_{\text{ph}}$) to analyze reported experimental TBC data²⁰⁻²³ for the MoS₂-SiO₂ interface and to discuss the possible physics underlying the variability of the TBC data. We also use the combined electronic and phononic BC results to predict the variability of the TBC for the WS₂-SiO₂ interface. Although the theoretical methods in this paper are used specifically to analyze the TBC variability of the single-layer MoS₂-SiO₂ and WS₂-SiO₂ interface, they can also be extended to other 2D crystals (e.g. graphene and other TMDs) and substrates (e.g. Al₂O₃).

II. THEORETICAL MODELS

We discuss our theoretical models of the phononic and electronic TBC processes, as depicted in the schematic of the TMD-substrate interface in Fig. 1, in the following subsections. Roughly speaking, we attribute the phononic TBC (G_{ph}) to the linear mechanical coupling between the flexural phonons of the TMD sheet and the bulk elastic waves (i.e., acoustic phonons) of the substrate, and the electronic TBC (G_{el}) to the remote scattering of the TMD electrons by the polar optical phonons of the dielectric substrate, also otherwise known as “remote phonon scattering”^{11,19}. We assume that the two TBC components are independent (i.e., the electron-phonon interaction has no effect on the mechanical coupling between the TMD and the substrate and vice versa) and can be added in parallel.

A. Heat dissipation from coherent and diffuse flexural phonon scattering

We adopt a linear elasticity theory-based approach to model the phononic TBC from Ref.⁸. Although the model is applied to the TMD-SiO₂ interface here, it is sufficiently general to be applied to any linear elastic isotropic substrate. The model, which assumes heat dissipation by coherent 2D flexural phonons at a *perfectly smooth interface*⁷, is used

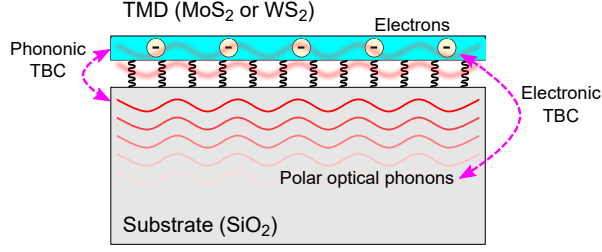


Figure 1. Schematic of the TMD-substrate interface and the phononic and electronic heat dissipation processes (represented by dashed lines). The TMD sheet is mechanically coupled to the SiO₂ substrate through the effective spring forces (represented by vertical wavy lines) at the interface while the TMD electrons (represented by circles) are coupled to the polar optical phonons (represented by horizontal wavy lines) in the substrate.

to derive the following expression for the *coherent* phononic TBC

$$G_{\text{ph}}^{\text{coh}} = \frac{1}{2\pi} \int_0^{\infty} d\omega \hbar\omega \frac{dN(\omega, T)}{dT} \Xi_{\text{coh}}(\omega), \quad (1)$$

where

$$\Xi_{\text{coh}}(\omega) = \frac{1}{(2\pi)^2} \int_{q < q_{\text{max}}} d^2q \frac{4K^2 \text{Im}D_{\text{sub}}(\mathbf{q}, \omega) \text{Im}D_{2\text{D}}(\mathbf{q}, \omega)}{|1 - K[D_{\text{sub}}(\mathbf{q}, \omega) + D_{2\text{D}}(\mathbf{q}, \omega)]|^2} \quad (2)$$

is the *coherent* areal transmission function, q_{max} is the maximum wave vector which we can set as $q_{\text{max}} = 2\pi/\sqrt{A} \approx 2 \times 10^{10} \text{ m}^{-1}$ (A is the unit cell area of the TMD), and $N(\omega, T) = [\exp(\frac{\hbar\omega}{k_B T}) - 1]^{-1}$ is the Bose-Einstein occupation factor at frequency ω and temperature T . The transmission function in Eq. (2) depends on the spring constant at the TMD-substrate interface K , the retarded Green's function for the flexural motion of the TMD monolayer $D_{2\text{D}}(\mathbf{q}, \omega)$, and the retarded Green's function for the free surface displacement of the isotropic solid substrate $D_{\text{sub}}(\mathbf{q}, \omega)$. The value of K for the MoS₂-SiO₂ interface is taken from Ref.⁸ while its value for the WS₂-SiO₂ interface is calculated using density functional theory like in Ref.⁸.

The expressions for $D_{2\text{D}}(\mathbf{q}, \omega)$ and $D_{\text{sub}}(\mathbf{q}, \omega)$ are⁸

$$D_{2\text{D}}(\mathbf{q}, \omega) = \lim_{\eta \rightarrow 0^+} [\rho\omega^2 + i\rho\gamma(\omega)\omega - \kappa q^4 + i\eta]^{-1} \quad (3)$$

where ρ and κ denote the areal mass density and the bending stiffness of the uncoupled 2D crystal, respectively, and

$$D_{\text{sub}}(\mathbf{q}, \omega) = \frac{i}{\rho_{\text{sub}} c_T^2} \frac{p_L(q, \omega)}{S(q, \omega)} \left(\frac{\omega}{c_T}\right)^2 \Theta(\omega_D - \omega) \quad (4)$$

where

$$S(q, \omega) = \left[\left(\frac{\omega}{c_T}\right)^2 - 2q^2 \right]^2 + 4q^2 p_T p_L, \quad (5a)$$

$$p_L(q, \omega) = \lim_{\eta \rightarrow 0^+} \left[\left(\frac{\omega}{c_L}\right)^2 - q^2 + i\eta \right]^{1/2}, \quad (5b)$$

$$p_T(q, \omega) = \lim_{\eta \rightarrow 0^+} \left[\left(\frac{\omega}{c_T}\right)^2 - q^2 + i\eta \right]^{1/2}, \quad (5c)$$

and c_L , c_T and ρ_{sub} are the longitudinal and transverse speed of sound, and the voluminal mass density of the substrate, respectively. In Eq. (4), $\Theta(\dots)$ represents the Heaviside function, and $\omega_D = (6\pi^2 N_{\text{sub}})^{1/3} c_L = 9.39 \times 10^{13} \text{ rad/s}$ (or 61.8 meV) and $N_{\text{sub}} = 6.62 \times 10^{28} \text{ m}^{-3}$ are respectively the longitudinal Debye frequency and number density²⁴ of the substrate (amorphous SiO₂). As in Ref.⁸, $\gamma(\omega)$ in Eq. (3) is the frequency-dependent damping coefficient representing the *intrinsic* damping of the flexural motion, given as $\gamma(\omega) = \frac{\omega T}{\alpha T_{\text{RT}}}$ where α is the ratio of the phonon lifetime to its

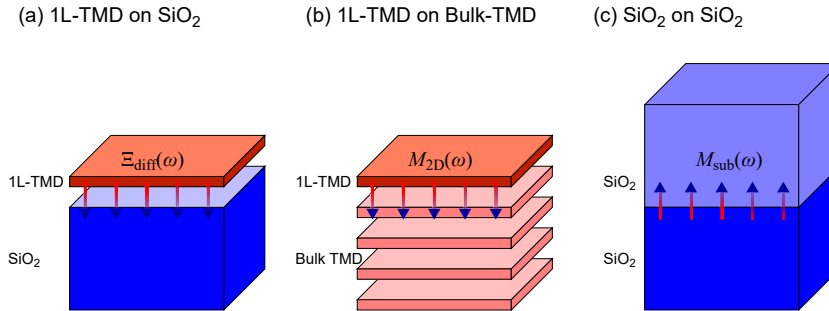


Figure 2. Schematic of the interfacial configurations used to determine (a) the diffuse phonon transmission function $\Xi_{\text{diff}}(\omega)$ between a 1-layer TMD crystal ('1L-TMD') and a SiO_2 substrate, (b) the number of modes $M_{2\text{D}}(\omega)$ between a 1L-TMD and a bulk TMD substrate, and (c) the number of modes $M_{\text{sub}}(\omega)$ between two semi-infinite SiO_2 solids.

period at room temperature and T_{RT} is the room temperature (300 K). It has been shown⁸ that it is necessary to include the intrinsic damping of the flexural motion in Eq. (3) to account for the interfacial heat dissipation correctly.

Although the predictions of the coherent flexural phonon model are relatively accurate for graphene^{8,9}, its predictions for the MoS_2 - SiO_2 interface are substantially smaller than experimental data^{21,22}, highlighting a possible shortcoming of the model. The theory in Eq. (2) assumes a perfectly smooth interface⁷ which limits energy transfer to processes that conserve parallel momentum, a restriction that may not apply to the more disordered TMD-substrate interface which can have surface roughness, trapped charged impurities and surface adsorbates²⁵. For a highly disordered interface, this assumption can be relaxed and we may assume that each incoming phonon is scattered by the disordered interface without constraints to all available outgoing phonon modes with *equal probability* like in the diffuse mismatch model (DMM)²⁶. Using this assumption, we apply the DMM approximation to modify Eq. (1) by writing the diffuse transmission function between the 2D crystal and the substrate as²⁷

$$\Xi_{\text{diff}}(\omega) = \frac{M_{2\text{D}}(\omega)M_{\text{sub}}(\omega)}{M_{2\text{D}}(\omega) + M_{\text{sub}}(\omega)}, \quad (6)$$

where $M_{2\text{D}}(\omega)$ and $M_{\text{sub}}(\omega)$ are the number of available transmitting modes per unit area at frequency ω in the 2D crystal and substrate, respectively. We stress that Eq. (6) describes a *phenomenological* model derived from purely kinetic considerations of detailed balance^{26,27} and ignores the details of the interactions at the interface. The corresponding TBC is

$$G_{\text{ph}}^{\text{diff}} = \frac{1}{2\pi} \int_0^\infty d\omega \hbar\omega \frac{dN(\omega, T)}{dT} \Xi_{\text{diff}}(\omega). \quad (7)$$

To determine $\Xi_{\text{diff}}(\omega)$ in Eq. (6), we need to count the number of modes in the 2D crystal and the substrate that contribute to cross-plane phonon transport at each frequency ω . This problem is particularly tricky for a single-layer 2D crystal since it has no extended volume in the cross-plane direction as shown in Fig. 2(a). Instead, we *estimate* $M_{2\text{D}}(\omega)$ in our model phenomenologically by assuming that the interface between the 2D crystal and a substrate consisting of a semi-infinite number of the same 2D material is acoustically transparent, e.g. a single-layer MoS_2 (1L- MoS_2) on a bulk MoS_2 ($\lim_{N \rightarrow \infty} N\text{L-}\text{MoS}_2$) substrate, such that the transmission function between the two materials is equal to the number of transmitting modes in the single-layer 2D crystal. To do this, we make the replacement $K \rightarrow K_{2\text{D}}$ and $D_{\text{sub}}(\mathbf{q}, \omega) \rightarrow D_{2\text{D}, \infty}(\mathbf{q}, \omega)$ in Eq. (2), where

$$D_{2\text{D}, \infty}(\mathbf{q}, \omega) = \Theta(z)D_+(\mathbf{q}, \omega) + \Theta(-z)D_-(\mathbf{q}, \omega) \quad (8)$$

is the surface response function of a semi-infinite 2D layered substrate²⁸, with

$$D_{\pm}(\mathbf{q}, \omega) = \frac{2}{z(\mathbf{q}, \omega) \pm \sqrt{z(\mathbf{q}, \omega)^2 - 4z(\mathbf{q}, \omega)K_{2\text{D}}}}$$

for $z(\mathbf{q}, \omega) = \lim_{\gamma \rightarrow 0} D_{2\text{D}}(\mathbf{q}, \omega)^{-1} = \rho\omega^2 - \kappa q^4$, and $K_{2\text{D}}$ is the interlayer spring constant in the substrate. Hence, we obtain the expression analogous to Eq. (2), i.e.,

$$M_{2\text{D}}(\omega) = \frac{1}{(2\pi)^2} \int_{q < q_{\text{max}}} d^2q \frac{4K_{2\text{D}}^2 \text{Im}D_{2\text{D}, \infty}(\mathbf{q}, \omega) \text{Im}D_{2\text{D}}(\mathbf{q}, \omega)}{|1 - K_{2\text{D}}[D_{2\text{D}, \infty}(\mathbf{q}, \omega) + D_{2\text{D}}(\mathbf{q}, \omega)]|^2} \quad (9)$$

TMD	WS ₂	MoS ₂
K (10 ¹⁹ Nm ⁻³)	6.12	4.94
κ (eV)	11.25 ²⁹	9.61 ²⁹
ρ (10 ⁻⁷ kgm ⁻²)	47.9	31.3
α	100 ⁸	
ρ_{sub} (kgm ⁻³)	2200 ⁷	
c_L (ms ⁻¹)	5953 ⁷	
c_T (ms ⁻¹)	3743 ⁷	
ω_D (meV)	61.8	
K_{2D} (10 ¹⁹ Nm ⁻³)	9.55 ³⁰	8.90 ³⁰

Table I. Parameters in our numerical simulations of Eqs. (1) and (7). K , which depends on the type of 2D crystal, is the spring constant per unit area for the OH-terminated SiO₂ interface and is calculated using DFT⁸. κ and ρ are respectively the intrinsic bending rigidity and mass density per unit area of the 2D crystal used in Eq. (3). K_{2D} is the spring constant per unit area for the bulk version of the 2D crystal³⁰.

which can be evaluated numerically. The set up of the calculation for $M_{2D}(\omega)$ for a single-layer TMD (1L-TMD) is shown in Fig. 2(b). In the case of SiO₂ as shown in Fig. 2(c), we estimate the number of modes per unit area in an isotropic elastic substrate $M_{\text{sub}}(\omega)$ as

$$M_{\text{sub}}(\omega) = \frac{\omega^2}{4\pi} \left(\frac{1}{c_L^2} + \frac{2}{c_T^2} \right) \Theta(\omega_D - \omega). \quad (10)$$

Since $M_{2D}(\omega) \ll M_{\text{sub}}(\omega)$ for $\omega < \omega_D$, we have $\Xi_{\text{diff}}(\omega) \approx M_{2D}(\omega)\Theta(\omega_D - \omega)$ and Eq. (7) becomes

$$G_{\text{ph}}^{\text{diff}} \approx \frac{1}{2\pi} \int_0^{\omega_D} d\omega \hbar\omega \frac{dN(\omega, T)}{dT} M_{2D}(\omega) \quad (11)$$

which depends on the substrate through its longitudinal Debye frequency ω_D and the 2D crystal through $M_{2D}(\omega)$. The expression in Eq. (11) suggests that in the diffuse limit, the phononic TBC for a particular 2D crystal can be maximized only through ω_D which depends on c_L . Hence, the phononic TBC would be high for hard insulators such as diamond and sapphire for which $c_L = 17500$ and 10890 m/s, respectively²⁶.

B. Heat dissipation by remote phonon scattering

To model the electronic TBC G_{el} , we use the theory developed in Ref.¹⁹. The expression for G_{el} is written as a 2D integral that can be evaluated numerically, i.e.,

$$G_{\text{el}} = \sum_{\gamma=\text{SO1,SO2}} \mathcal{F}_{\gamma} \int_0^{q_{\text{max}}} dq \frac{\exp(-2qd)}{\varepsilon(q)} \int_0^{\infty} d\mu' \frac{\text{Im}\mathcal{P}(\mathbf{q}, \omega_{\gamma}; \mu', 0)}{4k_B T \cosh^2\left(\frac{\mu-\mu'}{2k_B T}\right)} \quad (12)$$

where $q_{\text{max}} = 2 \times 10^{10} \text{ m}^{-1}$ is the cutoff wave vector like in Eq. (2), ω_{γ} is the frequency of the γ phonon, d is the TMD-substrate gap size, μ is the chemical potential, and

$$\mathcal{F}_{\gamma} = \frac{e^2 \hbar^2 \omega_{\gamma}^3}{\pi k_B T^2} [N(\omega_{\gamma}, T) + 1] N(\omega_{\gamma}, T) \left(\frac{1}{\epsilon_{\gamma, \text{hi}}} - \frac{1}{\epsilon_{\gamma, \text{lo}}} \right). \quad (13)$$

In Eq. (12), $\mathcal{P}(\mathbf{q}, \omega_{\gamma}; \mu, T)$ is the electron polarizability¹⁹ while the screening function $\varepsilon(q)$ is given by³¹

$$\varepsilon(q)^{-1} = 1 + \frac{e^2 \text{Re}\mathcal{P}(\mathbf{q}, 0; \mu, T)}{2\epsilon_0 q} \left[1 - \frac{\epsilon_{\text{sub}}^{\infty} - \epsilon_0}{\epsilon_{\text{sub}}^{\infty} + \epsilon_0} \exp(-2qd) \right] \quad (14)$$

where e and ϵ_0 are the electron charge and the permittivity of vacuum, respectively. In Eq. (13), the expressions for $\epsilon_{\text{SO1}, \text{hi}}$, $\epsilon_{\text{SO1}, \text{lo}}$, $\epsilon_{\text{SO2}, \text{hi}}$ and $\epsilon_{\text{SO2}, \text{lo}}$ are given by $\epsilon_{\text{SO1}, \text{hi}} = \frac{1}{2} \left[\epsilon_{\text{sub}}^{\infty} \left(\frac{\omega_{\text{LO2}}^2 - \omega_{\text{SO1}}^2}{\omega_{\text{TO2}}^2 - \omega_{\text{SO1}}^2} \right) + \epsilon_0 \right]$, $\epsilon_{\text{SO1}, \text{lo}} = \frac{1}{2} \left[\epsilon_{\text{sub}}^{\infty} \left(\frac{\omega_{\text{LO1}}^2}{\omega_{\text{TO1}}^2} \right) \left(\frac{\omega_{\text{LO2}}^2 - \omega_{\text{SO1}}^2}{\omega_{\text{TO2}}^2 - \omega_{\text{SO1}}^2} \right) + \epsilon_0 \right]$, $\epsilon_{\text{SO2}, \text{hi}} = \frac{1}{2} \left[\epsilon_{\text{sub}}^{\infty} \left(\frac{\omega_{\text{LO1}}^2 - \omega_{\text{SO2}}^2}{\omega_{\text{TO1}}^2 - \omega_{\text{SO2}}^2} \right) + \epsilon_0 \right]$ and $\epsilon_{\text{SO2}, \text{lo}} = \frac{1}{2} \left[\epsilon_{\text{sub}}^{\infty} \left(\frac{\omega_{\text{LO2}}^2}{\omega_{\text{TO2}}^2} \right) \left(\frac{\omega_{\text{LO1}}^2 - \omega_{\text{SO2}}^2}{\omega_{\text{TO1}}^2 - \omega_{\text{SO2}}^2} \right) + \epsilon_0 \right]$

Substrate	WS ₂	MoS ₂
m_e/m_0	0.31	0.51
d (Å)	3.0 ¹⁹	
g_s	2	
g_v	2	
$\epsilon_{\text{sub}}^\infty/\epsilon_0$	2.50	
$\epsilon_{\text{sub}}^i/\epsilon_0$	3.05	
$\epsilon_{\text{sub}}^0/\epsilon_0$	3.90	
ω_{TO1} (meV)	55.60	
ω_{TO2} (meV)	138.10	
ω_{SO1} (meV)	60.99	
ω_{SO2} (meV)	148.97	

Table II. Remote phonon scattering simulation parameters for WS₂ and MoS₂³². The effective electron masses m_e are expressed in terms of the free electron mass m_0 and taken from Ref.³². The variables m_e , g_s and g_v are used in $\mathcal{P}(\mathbf{q}, \omega_\gamma; \mu, T)$. The parameters $\epsilon_{\text{sub}}^\infty$, ϵ_{sub}^i , ϵ_{sub}^0 , ω_{TO1} and ω_{TO2} for SiO₂ are taken from Ref.³³.

where ω_{TO1} and ω_{TO2} are the transverse optical phonon frequencies associated with the bulk polar optical phonons of the substrate.

We use the simulation parameters from Table II for our G_{el} calculations. The longitudinal optical (LO) phonon frequencies ω_{LO1} and ω_{LO2} are determined from the zeros of $\epsilon_{\text{sub}}(\omega) = \epsilon_{\text{sub}}^\infty + (\epsilon_{\text{sub}}^i - \epsilon_{\text{sub}}^\infty) \frac{\omega_{\text{TO2}}^2}{\omega^2 - \omega_{\text{TO2}}^2} + (\epsilon_{\text{sub}}^0 - \epsilon_{\text{sub}}^i) \frac{\omega_{\text{TO1}}^2}{\omega^2 - \omega_{\text{TO1}}^2}$ while the surface optical (SO) phonon frequencies ω_{SO1} and ω_{SO2} are determined from solving $\epsilon_{\text{sub}}(\omega) + \epsilon_0 = 0$ ¹³.

III. NUMERICAL RESULTS AND DISCUSSION

A. Comparison of coherent and diffuse phononic TBC

It is intuitively expected that disorder in the interface leads to higher thermal resistance because of increased phonon scattering³⁴. However, the presence of interfacial disorder can enlarge the scattering phase space and possibly improve interfacial thermal transport by allowing energy transfer to proceed through scattering pathways that do not conserve parallel momentum³⁵. This difference in scattering is manifested in the transmission spectra $\Xi_{\text{coh}}(\omega)$ and $\Xi_{\text{diff}}(\omega)$ from Eqs. (2) and (6) in Fig. 3(a) which shows a marked difference in the transmission spectra for the MoS₂-SiO₂ interface, especially at low frequencies ($\omega < 12$ meV) where $\Xi_{\text{diff}}(\omega)$ is substantially higher than $\Xi_{\text{coh}}(\omega)$. The sharp drop in the transmission spectra observed at 61.8 meV is due to the frequency cutoff at the longitudinal Debye frequency of the substrate.

To understand the implications of the difference in the transmission spectra between the ordered and disordered TMD-substrate interface, we compare $G_{\text{ph}}^{\text{coh}}$ and $G_{\text{ph}}^{\text{diff}}$ of Eqs. (1) and (7) from $T = 100$ to 600 K, using the parameters in Table I, for the WS₂-SiO₂ and MoS₂-SiO₂ interface in Fig. 3(b). For the MoS₂-SiO₂ interface at $T = 300$ K, we obtain $G_{\text{ph}}^{\text{diff}} = 13.5$ MW/K/m², which is significantly larger than $G_{\text{ph}}^{\text{coh}} = 3.1$ MW/K/m² and more comparable to the value of $G = 14.0 \pm 3.7$ MW/K/m² at 311 K in Ref.²¹, $G = 20.3$ – 33.5 MW/K/m² at 295 K in Ref.²³, $G = 21.0$ MW/K/m² at 300 K in Ref.³⁶ and $G = 18.6$ MW/K/m² at 300 K in Ref.³⁷. This suggests that the MoS₂-SiO₂ interface is disordered, possibly connected to the absence of long-range order in a-SiO₂ and chemical inhomogeneity of its surface²⁵, and that its thermal transport properties are better described by the diffuse phonon model. The larger $G_{\text{ph}}^{\text{diff}}$ for the MoS₂-SiO₂ interface is also closer to classical MD simulation results ($G = 15.6$ MW/K/m² in Ref.²³, $G = 12.2$ – 23.5 MW/K/m² in Ref.³⁸ and $G = 25.6 \pm 3.3$ MW/K/m² in Ref.⁶). For the WS₂-SiO₂ interface at 300 K, we also find that $G_{\text{ph}}^{\text{diff}} = 12.4$ MW/K/m² is significantly larger than $G_{\text{ph}}^{\text{coh}} = 3.0$ MW/K/m². The good agreement of $G_{\text{ph}}^{\text{diff}}$ with experimentally derived values for the MoS₂-SiO₂ interface suggests that the real TBC value for the WS₂-SiO₂ interface is probably closer to the predicted $G_{\text{ph}}^{\text{diff}} = 12.4$ MW/K/m². We also note that the $G_{\text{ph}}^{\text{coh}}$ and $G_{\text{ph}}^{\text{diff}}$ values for the WS₂-SiO₂ and MoS₂-SiO₂ interface are comparable because of their similar elasticity parameters (ρ , κ and K_{2D}).

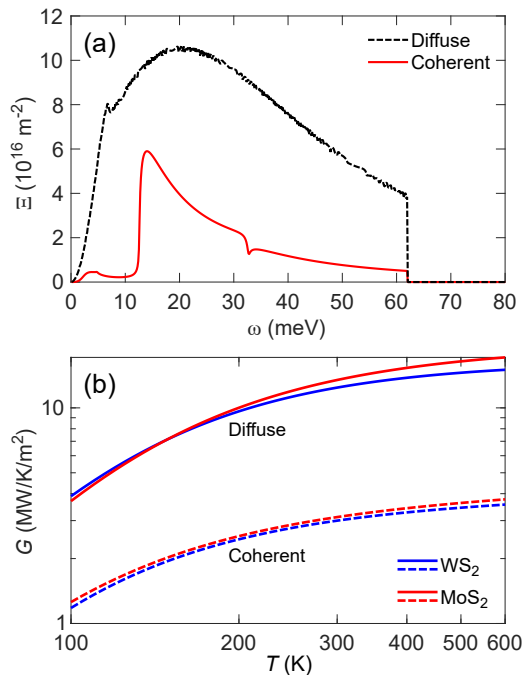


Figure 3. (a) Coherent and diffuse phonon transmission spectra for the MoS₂-SiO₂ interface at 300 K from Eqs. (2) and (6), respectively. (b) Temperature dependence of the coherent (dotted lines) and the diffuse (solid lines) phononic TBC ($G_{\text{ph}}^{\text{coh}}$ vs. $G_{\text{ph}}^{\text{diff}}$) for the WS₂-SiO₂ (blue lines) and MoS₂-SiO₂ (red lines) interface from $T = 100$ to 600 K. At 300 K, we have $G_{\text{ph}}^{\text{coh}} = 3.1$ MW/K/m² and $G_{\text{ph}}^{\text{diff}} = 13.5$ MW/K/m² ($G_{\text{ph}}^{\text{coh}} = 3.0$ MW/K/m² and $G_{\text{ph}}^{\text{diff}} = 12.4$ MW/K/m²) for the MoS₂-SiO₂ (WS₂-SiO₂) interface.

B. Interpretation of experimental data for MoS₂-SiO₂ interface

We combine the results for G_{el} , $G_{\text{ph}}^{\text{coh}}$ and $G_{\text{ph}}^{\text{diff}}$ to analyze the experimental TBC data (G_{expt}) for the MoS₂-SiO₂ interface from Yalon et al.²¹. As mentioned earlier, we assume that the phononic and electronic TBC components are independent and can be added in parallel, and that the electronic TBC is unaffected by the disorder at the TMD-substrate interface. In Fig. 4, we plot $G_{\text{ph}}^{\text{coh}}$, $G_{\text{ph}}^{\text{diff}}$, $G_{\text{ph}}^{\text{coh}} + G_{\text{el}}$ (coherent phononic and electronic) and $G_{\text{ph}}^{\text{diff}} + G_{\text{el}}$ (diffuse phononic and electronic) at different values of the electron density from $n = 10^{11}$ to 10^{12} cm⁻² in steps of $\Delta n = 10^{11}$ cm⁻² as a function of temperature and compare them to the G_{expt} data.

At $n = 0$ cm⁻², there is no electronic contribution to the overall TBC and the theoretical TBC values are given by $G_{\text{ph}}^{\text{coh}}$ or $G_{\text{ph}}^{\text{diff}}$ which we can treat as the baseline TBC. We find that the G_{expt} values are significantly higher than $G_{\text{ph}}^{\text{coh}}$ and in much closer agreement with $G_{\text{ph}}^{\text{diff}}$ over the temperature range of 311 to 558 K. This suggests that the diffuse phonon model captures the essential physics of heat dissipation at the MoS₂-SiO₂ interface and that electronic contribution to the TBC is not reflected in the G_{expt} data.

Nonetheless, we explore the effects of the electronic contribution to the total TBC which can be significant. Figure 4 shows that G_{expt} data can also be fitted by $G_{\text{ph}}^{\text{coh}} + G_{\text{el}}$ at $n = 0.3 \times 10^{12}$ cm⁻², i.e., the discrepancies between the experimental TBC data and the predicted coherent phononic TBC ones can be eliminated by adding the contribution from the remote phonon scattering of TMD electrons. Although the predictions for $G_{\text{ph}}^{\text{coh}} + G_{\text{el}}$ at the relatively low electron density of $n = 0.3 \times 10^{12}$ cm⁻² seem to fit the G_{expt} data slightly better at higher temperatures than the $G_{\text{ph}}^{\text{diff}}$ predictions do, the error bars in the G_{expt} data are too large for us to exclude $G_{\text{ph}}^{\text{coh}}$ or $G_{\text{ph}}^{\text{diff}}$ as the phononic component of the total TBC. Nonetheless, we favor $G_{\text{ph}}^{\text{diff}}$ as the phononic component because its predicted values are closer to classical MD simulation results^{6,23,38} which have no electronic contribution.

The substantial spread in the $G_{\text{ph}}^{\text{diff}} + G_{\text{el}}$ predictions in the $n = 0$ to 10^{12} cm⁻² range may also explain the variation in the experimental TBC values for the MoS₂-SiO₂ interface. It has been reported that the intrinsic doping of single-layer MoS₂ can reach up to $\sim 10^{13}$ cm⁻² on SiO₂ substrates^{39,40} although not all the electrons are delocalized⁴¹. In samples grown by chemical vapor deposition, a maximum electron density of $n \approx 10^{13}$ cm⁻² can be reached using an applied gate voltage⁴². Nonetheless, we limit our analysis in the following discussion to a conservative $n \leq 10^{12}$ cm⁻² range as there has not been any systematic attempt to measure how the TBC varies with n . As n increases from 0

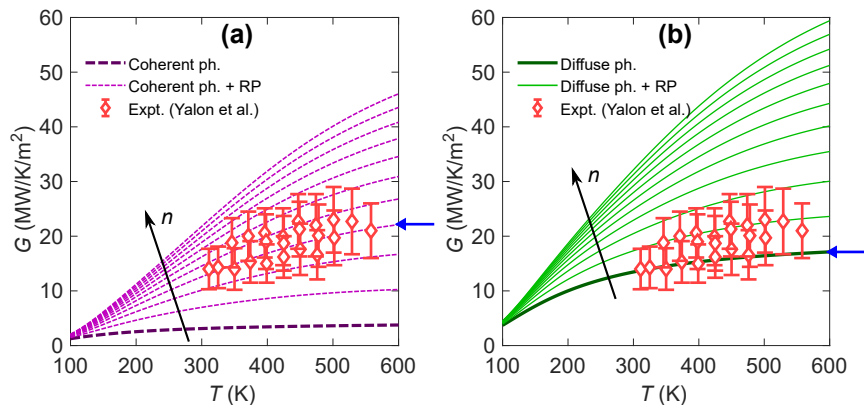


Figure 4. Temperature dependence of (a) $G_{\text{ph}}^{\text{coh}}$ (thick dashed line labeled ‘Coherent ph.’) and $G_{\text{ph}}^{\text{coh}} + G_{\text{el}}$ (fine purple dashed lines labeled ‘Coherent ph. + RP’), and (b) $G_{\text{ph}}^{\text{diff}}$ (thick solid line labeled ‘Diffuse ph.’) and $G_{\text{ph}}^{\text{diff}} + G_{\text{el}}$ (fine green solid lines labeled ‘Diffuse ph. + RP’) for the MoS₂-SiO₂ interface at different values of the electron density between $n = 10^{11}$ to 10^{12} cm⁻² in steps of $\Delta n = 10^{11}$ cm⁻². As n increases, so do $G_{\text{ph}}^{\text{coh}} + G_{\text{el}}$ and $G_{\text{ph}}^{\text{diff}} + G_{\text{el}}$ as indicated by the black arrow. The corresponding experimental TBC data from Yalon et al.²¹ are indicated by red diamond symbols with error bars. The $G_{\text{ph}}^{\text{coh}} + G_{\text{el}}$ ($n = 3 \times 10^{11}$ cm⁻²) and $G_{\text{ph}}^{\text{diff}} + G_{\text{el}}$ ($n = 0$ cm⁻²) curves that best fit the experimental data are indicated by the short blue arrows.

to 10^{12} cm⁻², the theoretical $G_{\text{ph}}^{\text{diff}} + G_{\text{el}}$ TBC at 300 K increases from 13.5 to 32.1 MW/K/m², producing a spread comparable to the TBC variation ($G = 20.3$ to 33.5 MW/K/m²) obtained at 295 K in Ref.²³. This suggests that the spread in TBC values may be caused by the variability in the electron density due to intrinsic doping in MoS₂⁴³ which is often n -doped as a result of sulfur atom vacancies⁴¹. It also implies that it should be possible to increase the TBC of the MoS₂-SiO₂ interface by doping the MoS₂ through the introduction of dopants^{44,45} or the use of a metal gate electrode (as in a field-effect transistor) to modulate the electron density. In addition to the change in the TBC as n increases, another striking feature is the change in the temperature dependence of the TBC.

C. Phononic and electronic TBC for WS₂-SiO₂ interface

We also present the simulated electronic and phononic TBC for the WS₂-SiO₂ interface in Fig. 5 in which we plot $G_{\text{ph}}^{\text{coh}}$, $G_{\text{ph}}^{\text{diff}}$, $G_{\text{ph}}^{\text{coh}} + G_{\text{el}}$ (coherent phononic and electronic) and $G_{\text{ph}}^{\text{diff}} + G_{\text{el}}$ (diffuse phononic and electronic) at different values of the electron density from $n = 10^{11}$ to 10^{12} cm⁻² in steps of $\Delta n = 10^{11}$ cm⁻² as a function of temperature. Unlike Fig. 4, no comparison with experimental data is made because no such data is available for the WS₂-SiO₂ interface. Nevertheless, the data in Fig. 5 can be useful for comparison with future experimental TBC measurements of the WS₂-SiO₂ interface and understanding its TBC variability.

We observe similar trends in Fig. 5 to the data in Fig. 4. At 300 K, as n increases from 0 to 10^{12} cm⁻², $G_{\text{ph}}^{\text{coh}} + G_{\text{el}}$ increases from 3.0 to 18.6 MW/K/m² while $G_{\text{ph}}^{\text{diff}} + G_{\text{el}}$ increases from 12.4 to 28.1 MW/K/m². We note that the $G_{\text{ph}}^{\text{coh}}$, $G_{\text{ph}}^{\text{diff}}$ and G_{el} data for the WS₂-SiO₂ interface are comparable but smaller than their corresponding values for the MoS₂-SiO₂ interface in Fig. 4. The large change in the $G_{\text{ph}}^{\text{coh}} + G_{\text{el}}$ and $G_{\text{ph}}^{\text{diff}} + G_{\text{el}}$ data with respect to n means that a change in electron density, from either intrinsic doping or an applied gate voltage, can also lead to a significant detectable change in the measured TBC as with the MoS₂-SiO₂ interface.

IV. SUMMARY AND CONCLUSION

In this work, we analyze the theoretical phononic and electronic TBC of the WS₂-SiO₂ and MoS₂-SiO₂ interface. To describe the phononic TBC contribution for the disordered TMD-substrate interface, we introduce a diffuse phonon model. We compare the coherent and diffuse phonon models for the WS₂-SiO₂ and MoS₂-SiO₂ interface, and find that the diffuse phonon model yields significantly higher TBC values that fit the TBC data for the MoS₂-SiO₂ interface from molecular dynamics simulations and thermometric experiments better, implying that the TMD-substrate interfaces are disordered. Our analysis of the experimental TBC data from Ref.²¹ for the MoS₂-SiO₂ interface indicates that the overall TBC is dominated by diffuse phonon transport although the electronic contribution from remote phonon

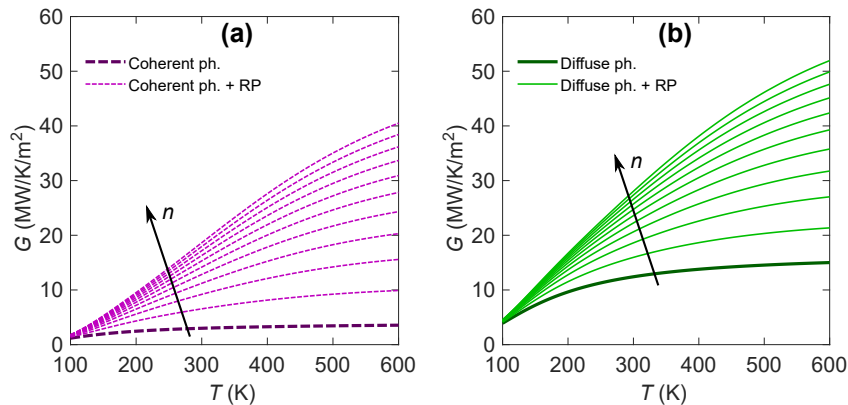


Figure 5. Temperature dependence of (a) $G_{\text{ph}}^{\text{coh}}$ (thick dashed line labeled ‘Coherent ph.’) and $G_{\text{ph}}^{\text{coh}} + G_{\text{el}}$ (fine purple dashed lines labeled ‘Coherent ph. + RP’) and (b) $G_{\text{ph}}^{\text{diff}}$ (thick solid line labeled ‘Diffuse ph.’) and $G_{\text{ph}}^{\text{diff}} + G_{\text{el}}$ (fine green solid lines labeled ‘Diffuse ph. + RP’) for the $\text{WS}_2\text{-SiO}_2$ interface at different values of the electron density between $n = 10^{11}$ to 10^{12} cm^{-2} in steps of $\Delta n = 10^{11}$ cm^{-2} . As n increases, so do $G_{\text{ph}}^{\text{coh}} + G_{\text{el}}$ and $G_{\text{ph}}^{\text{diff}} + G_{\text{el}}$ as indicated by the black arrow.

scattering can be significant even at low electron densities and becomes comparable to the phononic contribution at higher electron densities. The simulated phononic and electronic TBC data for the $\text{WS}_2\text{-SiO}_2$ interface also indicate that the electronic contribution to its TBC is also significant. Our results show that the spread in experimental TBC values of the $\text{MoS}_2\text{-SiO}_2$ interface can possibly be explained by the variability in intrinsic doping which affects the electronic TBC.

ACKNOWLEDGMENTS

We gratefully acknowledge support from the Science and Engineering Research Council through grant (152-70-00017) and use of computing resources at the A*STAR Computational Resource Centre and National Supercomputer Centre, Singapore. We also thank Eilam Yalon (Technion, Israel Institute of Technology) for sharing the experimental data from Ref.²¹ with us.

* ongzy@ihpc.a-star.edu.sg

- ¹ X. Li, L. Yang, M. Si, S. Li, M. Huang, P. Ye, and Y. Wu, *Advanced Materials* **27**, 1547 (2015).
- ² D. Lembke, S. Bertolazzi, and A. Kis, *Accounts of Chemical Research* **48**, 100 (2015).
- ³ E. Pop, *Nano Research* **3**, 147 (2010).
- ⁴ Z.-Y. Ong and M.-H. Bae, *2D Materials* **6**, 32005 (2019).
- ⁵ Z.-Y. Ong, B. Qiu, S. Xu, X. Ruan, and E. Pop, *J. Appl. Phys.* **123**, 115107 (2018).
- ⁶ S. V. Suryavanshi, A. J. Gabourie, A. Barati Farimani, and E. Pop, *J. Appl. Phys.* **126**, 55107 (2019).
- ⁷ B. N. J. Persson, A. I. Volokitin, and H. Ueba, *J. Phys.: Condens. Matter* **23**, 45009 (2011).
- ⁸ Z.-Y. Ong, Y. Cai, and G. Zhang, *Phys. Rev. B* **94**, 165427 (2016).
- ⁹ Z.-Y. Ong, *Phys. Rev. B* **95**, 155309 (2017).
- ¹⁰ G. C. Correa, C. J. Foss, and Z. Aksamija, *Nanotechnology* **28**, 135402 (2017).
- ¹¹ K. Hess and P. Vogl, *Solid State Communications* **30**, 797 (1979).
- ¹² M. V. Fischetti, D. A. Neumayer, and E. A. Cartier, *J. Appl. Phys.* **90**, 4587 (2001).
- ¹³ A. Konar, T. Fang, and D. Jena, *Phys. Rev. B* **82**, 115452 (2010).
- ¹⁴ K. Zou, X. Hong, D. Keefer, and J. Zhu, *Phys. Rev. Lett.* **105**, 126601 (2010).
- ¹⁵ Z. Yu, Y. Pan, Y. Shen, Z. Wang, Z. Y. Ong, T. Xu, R. Xin, L. Pan, B. Wang, L. Sun, J. Wang, G. Zhang, Y. W. Zhang, Y. Shi, and X. Wang, *Nature Communications* **5**, 5290 (2014).
- ¹⁶ Z. Yu, Z.-Y. Ong, Y. Pan, Y. Cui, R. Xin, Y. Shi, B. Wang, Y. Wu, T. Chen, Y.-W. Zhang, G. Zhang, and X. Wang, *Advanced Materials* **28**, 547 (2016).
- ¹⁷ Z.-Y. Ong, M. V. Fischetti, A. Y. Serov, and E. Pop, *Phys. Rev. B* **87**, 195404 (2013).
- ¹⁸ Y. K. Koh, A. S. Lyons, M. H. Bae, B. Huang, V. E. Dorgan, D. G. Cahill, and E. Pop, *Nano Lett.* **16**, 6014 (2016), arXiv:1603.00358.
- ¹⁹ Z.-Y. Ong, G. Zhang, L. Cao, and Y.-W. Zhang, *Phys. Rev. Research* **2**, 033470 (2020).

- ²⁰ A. Taube, J. Judek, A. Lapinska, and M. Zdrojek, *ACS Appl. Mater. Interfaces* **7**, 5061 (2015).
- ²¹ E. Yalon, O. B. Aslan, K. K. H. Smithe, C. J. McClellan, S. V. Suryavanshi, F. Xiong, A. Sood, C. M. Neumann, X. Xu, K. E. Goodson, T. F. Heinz, and E. Pop, *ACS Appl. Mater. Interfaces* **9**, 43013 (2017).
- ²² E. Yalon, C. J. McClellan, K. K. H. Smithe, M. Munoz Rojo, R. L. Xu, S. V. Suryavanshi, A. J. Gabourie, C. M. Neumann, F. Xiong, A. B. Farimani, and E. Pop, *Nano Lett.* **17**, 3429 (2017).
- ²³ P. Yasaei, C. J. Foss, K. Karis, A. Behranginia, A. I. El-Ghandour, A. Fathizadeh, J. Olivares, A. K. Majee, C. D. Foster, F. Khalili-Araghi, Z. Aksamija, and A. Salehi-Khojin, *Advanced Materials Interfaces* **4**, 1700334 (2017).
- ²⁴ K. E. Goodson, M. I. Flik, L. T. Su, and D. A. Antoniadis, *J. Heat Transfer* **116**, 317 (1994).
- ²⁵ D. Rhodes, S. H. Chae, R. Ribeiro-Palau, and J. Hone, *Nature Materials* **18**, 541 (2019).
- ²⁶ E. T. Swartz and R. O. Pohl, *Rev. Mod. Phys.* **61**, 605 (1989).
- ²⁷ J. Zhang, C. A. Polanco, and A. W. Ghosh, *J. Heat Transfer* **140**, 092405 (2018), arXiv:1612.04807.
- ²⁸ Z.-Y. Ong, Y. Cai, G. Zhang, and Y.-W. Zhang, Submitted.
- ²⁹ K. Lai, W. B. Zhang, F. Zhou, F. Zeng, and B. Y. Tang, *J. Phys. D: Appl. Phys.* **49**, 185301 (2016).
- ³⁰ L. Liang, J. Zhang, B. G. Sumpter, Q. H. Tan, P. H. Tan, and V. Meunier, *ACS Nano* **11**, 11777 (2017).
- ³¹ Z.-Y. Ong and M. V. Fischetti, *Phys. Rev. B* **86**, 121409 (2012).
- ³² Z. Jin, X. Li, J. T. Mullen, and K. W. Kim, *Phys. Rev. B* **90**, 045422 (2014), arXiv:1406.4569.
- ³³ Z.-Y. Ong and M. V. Fischetti, *Phys. Rev. B* **86**, 165422 (2012).
- ³⁴ P. E. Hopkins, *ISRN Mechanical Engineering* **2013**, 682586 (2013).
- ³⁵ Z. Tian, K. Esfarjani, and G. Chen, *Phys. Rev. B* **86**, 235304 (2012).
- ³⁶ J. Guo, F. Yang, M. Xia, X. Xu, and B. Li, *J. Phys. D: Appl. Phys.* **52**, 385306 (2019).
- ³⁷ Y. Yu, T. Minhaj, L. Huang, Y. Yu, and L. Cao, *Physical Review Applied* **13**, 034059 (2020).
- ³⁸ H. Farahani, A. Rajabpour, M. Khanaki, and A. Reyhani, *Computational Materials Science* **142**, 1 (2018).
- ³⁹ B. W. Baugher, H. O. Churchill, Y. Yang, and P. Jarillo-Herrero, *Nano Lett.* **13**, 4212 (2013).
- ⁴⁰ K. F. Mak, K. He, C. Lee, G. H. Lee, J. Hone, T. F. Heinz, and J. Shan, *Nature Materials* **12**, 207 (2013).
- ⁴¹ H. Qiu, T. Xu, Z. Wang, W. Ren, H. Nan, Z. Ni, Q. Chen, S. Yuan, F. Miao, F. Song, G. Long, Y. Shi, L. Sun, J. Wang, and X. Wang, *Nature Communications* **4**, 2642 (2013).
- ⁴² K. K. Smithe, C. D. English, S. V. Suryavanshi, and E. Pop, *2D Materials* **4**, 011009 (2017).
- ⁴³ W. S. Leong, Y. Li, X. Luo, C. T. Nai, S. Y. Quek, and J. T. Thong, *Nanoscale* **7**, 10823 (2015).
- ⁴⁴ D. Kiriya, M. Tosun, P. Zhao, J. S. Kang, and A. Javey, *Journal of the American Chemical Society* **136**, 7853 (2014).
- ⁴⁵ P. Rastogi, S. Kumar, S. Bhowmick, A. Agarwal, and Y. S. Chauhan, *J. Phys. Chem. C* **118**, 30309 (2014).